Dalton Transactions

ROYAL SOCIETY OF CHEMISTRY

PAPER

View Article Online
View Journal

Cite this: DOI: 10.1039/d6dt01053a

Novel Fe_4 cluster topology from a new hexadentate chelate: magnetic analysis by experimental, DFT, and magnetostructural correlation methods

Alexander Diodati,[a] ChristiAnna L. Brantley,[a] Juan E. Peralta,[b] Amelia Figueroa,[a] Lukasz Dobrzycki,[a] Khalil A. Abboud[a] and George Christou *[a]

Received 5th May 2026,
Accepted 25th May 2026

DOI: 10.1039/d6dt01053a

rsc.li/dalton

The new potentially hexadentate chelate *N,N′*-bis(2-pyridylmethyl)-*N,N′*-bis(2-hydroxyethyl)-ethylenediamine ($bphnH_2$) has been synthesized. It possesses a mixed diol/diamine/dipyridine nature and has proven the source of two new Fe^{III}/oxo complexes with unprecedented structures. $[Fe_2O(bphnH)(bphnH_2)][Ce(NO_3)_6]$ (**1**) and $[Fe_4O(bphn)_2(NO_3)_4](NO_3)_2$ (**2**) contain pentadentate and hexadentate chelates, respectively. A three-pronged approach comprising fits of experimental magnetic susceptibility data, DFT computations and use of a magnetostructural correlation has been applied to analyse the variable-temperature magnetic properties of **2**, the reliability of obtained pairwise J_{ij} exchange interactions, the occurrence and avoidance of overparameterization problems, and the quantitative determination of a very weak long-range interaction in a molecule also containing very strong and medium strength interactions.

Introduction

Fe^{III}-oxo cluster chemistry is the foundation of many current areas of research, including molecular magnetism, single-molecule magnets, catalysis, bioinorganic chemistry, biomedical applications and others.[1–10] For example, dinuclear Fe^{III}-oxo clusters have been prepared as synthetic analogues of iron-based proteins and enzymes such as hemerythrin, methane monooxygenase, and ribonucleotide reductase.[11–20] Previous research in our group in Fe^{III}-oxo cluster chemistry has primarily been stimulated by its relevance to molecular magnetism and has involved the synthesis and characterization of a large range of compounds with nuclearities in the Fe_2–Fe_{36} range.[21] These were obtained from various synthetic routes, almost always involving a multidentate N,O-chelate such as 2-(hydroxymethyl)pyridine (hmpH), *N*-methyldiethanolamine ($mdaH_2$),[28] *N,N′*-bis(2-hydroxyethyl) ethylenediamine ($heenH_2$), 2-{[2-(dimethylamino)ethyl]-methylamino}ethanol (dmemH), and *N,N,N′,N′*-tetrakis(2-hydroxyethyl)ethylenediamine ($edteH_4$), to name but a few.[22–26] In addition, a given chelate can often give clusters of distinctly different metal nuclearities, as we very recently showed, for example, using $mdaH_2$ in similar reaction systems that nevertheless led to Fe^{III}-oxo cluster products comprising Fe_7, Fe_{22}, and Fe_{24} nuclearities.[27,28] Similar results have been found with $edteH_4$.[24]

The study of the magnetic properties of Fe^{III}-oxo clusters is the primary objective of our work, especially the determination of their ground state spin (S) and constituent pairwise Fe_2 magnetic exchange couplings, J_{ij}, the latter often allowing rationalization of the former. Fe^{III} is usually octahedral and high-spin (s = 5/2) in a wholly or predominantly O-based ligand field, leading to symmetric d-electron distribution and only small levels of magnetic anisotropy (zero-field splitting). Therefore, pairwise Fe_2 exchange interactions are almost always antiferromagnetic (AF) and readily obtained for low nuclearity (<Fe_8 typically) from fits of experimental magnetic susceptibility (χ_M) data. However, for low-symmetry Fe_n topologies with multiple independent couplings these can give excellent fits whose J_{ij} values are nevertheless unrelated to 'reality' due to overparameterization problems. Therefore, in parallel we also carry out DFT calculations of J_{ij} values as an independent check of experimental data, and as an additional independent approach we also calculate the predicted J_{ij} from a magnetostructural correlation (MSC) equation that employs the bridging Fe–O–Fe angles and Fe–O bond lengths;[29] we developed this Mitchell–Christou MSC specifically for higher nuclearity clusters once we realized that the Fe_2 MSC's already in the literature were of little use for higher nuclearities.

The above three-pronged approach has proven a very powerful and satisfying means of analyzing the magnetic properties of Fe^{III}-oxo clusters, currently up to Fe_{36} nuclearities, especially in identifying the presence of spin frustration effects within

[a]*Department of Chemistry, University of Florida, Gainesville, Florida 32611, USA. E-mail: christou@chem.ufl.edu*
[b]*Department of Physics, Central Michigan University, Mount Pleasant, Michigan 48859, USA*

triangular Fe_3 subunits and the relative spin vector alignments at each Fe^{III} ion.[30–35] This in turn allows rationalization of the cluster's often unexpected and unpredictable ground state *S*, which is normally a very challenging objective for higher nuclearity systems. Spin frustration is here defined in the way appropriate for molecular chemistry, namely, the presence of competing exchange interactions of comparable magnitude that prevent (frustrate) the preferred spin alignments of one or more of the constituent J_{ij} interactions; we prefer this definition over the original solid-state physics definition involving degenerate ground states, since the latter are very rarely encountered in malleable molecular systems.[8] Another important result of spin frustration is that if the resulting ground state *S* is large enough, Fe^{III}-oxo clusters can even function as single-molecule magnets (SMMs), such as the prototypical Fe_8 cluster, even though, as mentioned, they typically do not possess substantial magnetic anisotropy.[11] For all these reasons, we have continued to work in Fe^{III}-oxo cluster chemistry and are seeking new complexes of any Fe nuclearity in order (i) to expand the application of our three-pronged analytical approach; (ii) to increase our understanding of their magnetic structures; and (iii) to further probe the effectiveness of our MSC. We are therefore investigating new N,O chelates that could potentially yield new Fe^{III}-oxo nuclearities and/or topologies.

In the present work, we report the synthesis of a new chelate *N*,*N*′-bis(2-pyridylmethyl)-*N*,*N*′-bis(2-hydroxyethyl)ethylenediamine ($bphnH_2$) that can be considered a 'hybrid' of *N*,*N*,*N*′,*N*′-tetrakis(2-pyridinylmethyl)-1,2-ethanediamine (tpen) and $edteH_4$, thus combining the attributes of a polyalcohol, polyamine, and polypyridine into one hexadentate chelate (*vide infra*). We shall describe the synthesis of this new chelate, as well as its use to obtain an Fe_2 and an unusual Fe_4 complex, the latter possessing a novel Fe/O core. We shall also describe our synthetic methods, and the magnetic properties of these new complexes.

Experimental

Synthetic procedures

All reagents were used as received without further purification. All reactions were carried out under aerobic conditions unless otherwise noted.

***N*,*N*′-Bis(2-pyridylmethyl)-*N*,*N*′-bis(2-hydroxyethyl)ethylenediamine ($bphnH_2$).** To a stirred solution of 2-picoylchloride hydrochloride (4.92 g, 30.0 mmol) in deionized water (90 mL) was added dropwise an aqueous solution of sodium hydroxide (1.0 M, 30 mL) to yield a tan-coloured solution. To this was added *N*,*N*′-bis(2-hydroxyethyl)ethylenediamine (2.22 g, 30.0 mmol), which caused a colour change to light pink. The solution was stirred for 48 h at room temperature, during which time it became red, and then a second aliquot of aqueous sodium hydroxide (1.0 M, 30 mL) was added, turning the solution an intense red colour. The reaction was stirred a further 4 days at room temperature, during which time the solution became light orange.

The product was extracted from the aqueous solution with CH_2Cl_2 (5 × 100 mL aliquots) and the combined organic extracts were dried with anhydrous magnesium sulfate, filtered, and the filtrate concentrated under reduced pressure to give a deep red and extremely viscous oil of $bphnH_2$, which was used for synthesis without further purification. The yield was 2.98 g, 65%. ^{1}H NMR spectrum (400 MHz, $CDCl_3$), δ (ppm): 2.62 (t, 4H), 2.64 (s, 4H) 3.54 (t, 4H), 3.67 (s, 4H), 4.90 (s, 2H), 7.04–8.46 (m, 10H). Selected infra-red bands (KBr disc; cm^{-1}): 3276 (br), 2824 (w), 1651 (w), 1592 (s), 1569 (m), 1474 (m), 1433 (s), 1363 (w), 1150 (w), 1047 (s), 1001 (sh), 870 (w), 755 (vs), 617 (s).

$[Fe_2O(bphnH)(bphnH_2)][Ce(NO_3)_6]$ (1). To a stirred solution of $bphnH_2$ (0.23 g, 0.75 mmol) in MeOH (100.0 mL) was added NEt_3 (0.035 mL, 0.25 mmol) and $Fe(NO_3)_3{\cdot}9H_2O$ (0.303 g, 0.75 mmol), followed by $Ce(NO_3)_3{\cdot}6H_2O$ (0.34 g, 0.75 mmol) to give a light yellow-orange solution. This was heated at reflux for 30 min, allowed to cool, and left undisturbed for two days, during which time dark green, flower-shaped crystals of **1**·*x*MeOH had grown. These were collected by filtration, washed with cold MeOH, and dried under vacuum. The yield was 0.34 g, 33% based on Fe. Elemental analysis: calculated (found)% for **1**·2MeOH ($C_{38}H_{58}CeFe_2N_{14}O_{25}$): C, 33.49 (33.22); H, 4.29 (4.25); N, 14.39 (14.15). Selected infra-red bands (KBr disc; cm^{-1}): 1606 (w), 1572 (w), 1480 (sh), 1421 (m, br), 1363 (w), 1300 (m, br), 1284 (sh), 1160 (w), 1083 (w), 1046 (sh), 1026 (sh), 1021 (m), 975 (w), 955 (w), 914 (w), 882 (w), 817 (m), 768 (m), 733 (m), 718 (m), 648 (m), 423 (w).

$[Fe_4O(bphn)_2(NO_3)_4](NO_3)_2$ (2). To a solution of $bphnH_2$ (0.23 g, 0.75 mmol) in MeOH (100 mL) was added NEt_3 (0.105 mL, 0.75 mmol) followed by $Fe(NO_3)_3{\cdot}9H_2O$ (0.606 g, 1.50 mmol) to give a light orange solution. This was heated at reflux with stirring for 30 min, allowed to cool to room temperature, and then left undisturbed for two days for the solvent to partially evaporate slowly, during which time deep orange-red needle-like crystals of **2**·*x*MeOH had formed. The crystals for X-ray crystallography were kept in mother liquor, otherwise they were collected by filtration, washed with cold MeOH, and dried under vacuum. The yield was 0.36 g, 37% based on Fe. Elemental analysis: calculated (found)% for **2** ($C_{36}H_{48}Fe_4N_{14}O_{23}$): C, 34.09 (33.55); H, 3.81 (3.92); N, 15.46 (15.30). Selected infra-red bands (KBr disc; cm^{-1}): 1607 (m), 1570 (w), 1534 (m), 1483 (s), 1332 (s), 1280 (s), 1256 (s), 1152 (m), 1134 (sh), 1103 (w), 1085 (m), 1058 (m), 1022 (s), 991 (sh), 985 (m), 962 (sh), 913 (m), 888 (m), 802 (s), 778 (m), 763 (s), 754 (s), 732 (sh), 716 (m), 650 (s), 627 (s), 519 (sh), 497 (s), 448 (w).

X-ray crystallography

X-ray intensity data were collected at 100 K on a Bruker Dual micro source D8 Venture diffractometer and PHOTON III detector, running the APEX3 software package and using MoKα radiation (λ = 0.71073 Å). The data frames were integrated, and multi-scan scaling was applied in APEX3. Intrinsic phasing structure solution provided all the non-H atoms. The structures were refined on F^2 using full-matrix least-squares cycles. R_1 is calculated to provide a reference to the conven-

tional R value, but its function is not minimized (Table 1).[36,37] The non-H atoms were refined with anisotropic displacement parameters and all of the H atoms were placed in calculated idealized positions and refined as riding on their parent atoms.

For **1**·*x*MeOH, the asymmetric unit consists of the complete Fe_2 cation, a $[Ce(NO_3)_6]^{3-}$ anion, and disordered MeOH solvent molecules. The data were refined as a perfect inversion twin. The unbound CH_2CH_2OH arm of one bphnH$^-$ chelate is disordered and was refined in two parts. One MeOH solvent was slightly disordered and was refined in two parts, but the other MeOH molecules were too disordered to be modelled and program SQUEEZE was again used to remove the solvent disorder area of 66 Å^3 and 20 electrons. In the final refinement cycle, 12 512 reflections of which 11 576 are observed with $I > 2\sigma(I)$ were used to refine 687 parameters, and the resulting R_1, wR_2 and S were 3.73%, 9.68% and 1.025, respectively.

For **2**·*x*MeOH, the asymmetric unit contains the complete Fe_4 cation, two disordered NO_3^- anions, and disordered MeOH solvent molecules. One bphn^{2-} shows some disorder in its C and N atoms, and they were refined in two parts with isotropic thermal parameters. Three of the four NO_3^- ligands are disordered: the one on Fe3 was refined in two parts, whereas the two on Fe4 were each disordered 50% between a chelating and monodentate binding mode. The NO_3^- anions are also disordered and were refined in two or three parts with isotropic thermal parameters.

Solvent MeOH molecules were too disordered to be modelled, thus program SQUEEZE, part of the PLATON package of crystallographic software,[36,37] was used to calculate the solvent disorder area of 397 Å^3 and 39 electrons and remove its contribution to the overall intensity data. In the final refinement cycle, 14 089 reflections of which 11 640 are observed with $I > 2\sigma(I)$ were used to refine 644 parameters, and the resulting R_1, wR_2 and S were 6.79%, 20.28% and 1.083, respectively.

Table 1 Crystallographic data for complexes **1**·*x*MeOH and **2**·*x*MeOH

Parameters	**1**·*x*MeOH	**2**·*x*MeOH
Formula[a]	$C_{37}H_{50}CeFe_2N_{14}O_{24}$	$C_{36}H_{48}Fe_4N_{14}O_{23}$
F_W, g mol^{-1}	1326.73	1266.68
Crystal system	Orthorhombic	Triclinic
Space group	$P2_12_12_1$	$P\bar{1}$
a, Å	15.6614(3)	11.7197(6)
b, Å	16.9224(4)	15.6104(8)
c, Å	19.0128(4)	17.1367(9)
α, °	90	64.9490(1)
β, °	90	89.806(2)
γ, °	90	85.460(2)
Volume, Å^3	5038.93(19)	2829.7(3)
Z	4	2
ρ_{calc}, g cm^{-3}	1.749	1.487
μ, mm^{-1}	1.555	1.090
Temperature, K	100(2)	100(2)
Wavelength, Å[b]	0.71073	0.71073
Goodness-of-fit on F^2	1.025	1.083
R_1 [c]	0.0373	0.0679
wR_2 [d]	0.0968	0.2028
$(\Delta\rho)_{max,min}$ (e Å^{-3})	1.122, −0.492	3.013, −1323

[a] Excluding solvent molecules. [b] Graphite monochromator. [c] $I > 2\sigma(I)$, $R_1 = \sum(||F_o| - |F_c||)/\sum|F_o|$. [d] $wR_2 = [\sum[w(F_o^2 - F_c^2)^2]/\sum[w(F_o^2)^2]]^{1/2}$, $S = [\sum[w(F_o^2 - F_c^2)^2]/(n-p)]^{1/2}$, $w = 1/[\sigma^2(F_o^2) + (mp)^2 + np]$, $p = [\max(F_o^2,0) + 2F_c^2]/3$; m and n are constants.

Magnetochemistry

Variable-temperature direct current (DC) and alternating current (AC) magnetic susceptibility data on vacuum-dried samples of **1**·2MeOH and **2** were collected on a Quantum Design MPMS-XL superconducting quantum interference device (SQUID) magnetometer in the 1.8 to 300 K temperature range. Samples were prepared by lightly grinding the crystalline product into a powder and loading it into a capsule, restrained with eicosane to prevent torquing. The DC magnetic susceptibility (χ_M, as $\chi_M T$) data were measured in a 0.1 T (1000 G) applied field in the 5.0 to 300 K range and fit using program PHI.[38] In-phase (χ'_M) and out-of-phase (χ''_M) AC magnetic susceptibility data were measured in the 1.8 to 15.0 K range using a 3.5 G ac field at a 1000 Hz oscillation frequency. Pascal's constants were used to estimate the diamagnetic corrections for each compound,[39,40] and those for the eicosane and gel capsule were measured as a blank. The combined corrections were subtracted from the experimental susceptibilities to yield the molar paramagnetic susceptibilities.

Density functional theory (DFT) calculations

DFT calculations were carried out with an in-house version of the Gaussian 16 program that facilitates spin inversions at the paramagnetic atoms and was used to produce appropriate initial guesses for self-consistent broken spin-symmetry calculations.[41] The hybrid Perdew–Burke–Ernzerhof (PBEh) density functional approximation was employed. The PBEh functional admixes 25% of exact (Hartree–Fock-type) exchange and 75% of PBE exchange, and it is known to perform reasonably well for magnetic exchange couplings.[42–46] For example, for a set of eleven dinuclear oxo-bridged Fe^{III} complexes, PBEh predicted exchange couplings with an RMS error of approximately 10%.[47] In the present work, Pople's all-electron 6-311+G** basis set was used for Fe atoms and the 6-31G** for lighter elements.[48] Point group symmetry and relativistic effects were neglected in the DFT calculations and the spin model, and a self-consistency convergence threshold of 10^{-6} Ha = 0.2 cm^{-1} in the energy and 10^{-8} in the RMS changes in the density matrix were employed.

DFT calculations on **2** were performed using the unrelaxed X-ray crystallographic coordinates of **2**·*x*MeOH. A total of five independent nearest-neighbour exchange couplings, J_{ij}, were determined from DFT calculations using the broken-symmetry method. This utilized Ising-type spin configurations, S, which are mapped onto the broken-symmetry DFT solutions. The chosen configurations were all-parallel (high-spin), all four single-spin inversions, and all five first-neighbour two-spin inversions, giving a total of ten broken-symmetry solutions. The energies, $E(S)$, of the broken symmetry configurations are expressed in terms of a sum over spin interactions (eqn (1)),

$$E(S) = E_0 - 2\sum_{\langle ij \rangle} J_{ij} S_i \cdot S_j \quad (1)$$

where $\langle ij \rangle$ stands for all nearest-neighbour ij pairs, $S_k = \pm 5/2$ for Fe^{III}, and E_0 is a constant that offsets spin model and DFT energy spectra. The calculated energies $E(S)$ of the spin configurations S were then used in a linear regression to determine the five J_{ij} exchange couplings of eqn (1). This method has been employed numerous times in the literature for evaluating exchange couplings in multinuclear transition metal complexes.[42–46] The linear regression R^2 coefficient differs from 1 by less than 10^{-6}, which is a strong indication that the broken spin-symmetry DFT solutions are reliable representations of the Ising configurations.

Other studies

Infrared spectra in the 400–4000 cm^{-1} range were collected on KBr discs using a Nicolet iS5 FTIR spectrometer, with peaks reported with the following key: (br, broad; vs, very strong; s, strong; m, medium; w, weak; sh, shoulder). For organic compounds, NMR spectra were obtained using a Varian Unity Inova 400 MHz spectrometer at the University of Florida. Chemical shifts (δ, ppm) are referenced to the $CHCl_3$ solvent peak at 7.26 ppm for ^1H NMR and 77.16 ppm for ^{13}C NMR. The peak multiplicities are abbreviated as follows: s, singlet; d, doublet; t, triplet; q, quartet; m, multiplet. C/H/N elemental analyses were carried out by Atlantic Microlabs, Inc. in Norcross, Georgia.

Results and discussion

Syntheses

As stated, the new chelate $bphnH_2$ can be considered a hybrid of $edteH_4$ and tpen, as indicated diagrammatically in Scheme 1.

$EdteH_4$ and tpen are similar in both being hexadentate chelates and having an ethylenediamine backbone, but they are very different in an important way: $edteH_4$ has four alcohol arms that on deprotonation each generate powerful μ_n-bridging (n = 2, 3) alkoxide groups that can foster formation of higher nuclearity products such as $[Fe_{12}O_4(OH)_8(edte)_4(H_2O)_2](NO_3)_4$ [24] and $[Mn_{20}O_8(OH)_4(O_2CMe)_6(edte)_6]$.[49] In contrast, the four pyridyl arms of tpen can only function as monodentate ligands, and thus this chelate tends to either give mononuclear complexes or acts as a binucleating ligand giving dinuclear products such as $[Mn_2O_2(O_2CMe)(tpen)]^{2+}$ salts.[50] Therefore, we wondered what kind of products might result from a hybrid comprising two alcohol and two pyridyl arms on an ethylenediamine backbone, namely, $bphnH_2$. The latter has never been synthesized before to our knowledge; however, *N*-(2-pyridylmethyl)-2-aminoethanol (mpenH) is essentially half of $bphnH_2$ and has previously been shown to form mononuclear compounds.[51,52]

The synthesis of $bphnH_2$ was related to those for tpen and mpenH, and involved the addition of *N*,*N*′-bis(2-hydroxyethyl) ethylenediamine to an aqueous solution of 2-picoylchloride hydrochloride neutralized with 1.0 M aqueous NaOH. After 2 days at room temperature, a second aliquot of 1.0 M aqueous NaOH was added, the reaction left for a further 4 days, and the product extracted using CH_2Cl_2. The solvent was removed *in vacuo*, affording 2.98 g of a thick viscous red oil of $bphnH_2$ in ~65% yield. The red oil was used as is without further purification. The overall reaction is summarized in Scheme 2.

The reaction of $Fe(NO_3)_3$ with $bphnH_2$, $Ce(NO_3)_3$ and NEt_3 in a 3 : 3 : 1 : 1 molar ratio in refluxing MeOH led to a light yellow-orange solution from which was subsequently isolated $[Fe_2O(bphnH)(bphnH_2)][Ce(NO_3)_6]$ (**1**) in 33% yield and high purity. This procedure was initially developed to target heterometallic Fe/Ce clusters, and with the identity of **1** established we explored if we could isolate the cation as the NO_3^- or ClO_4^- salt. Only the latter gave an isolable crystalline product, but as poorly diffracting crystals in low yield (9%). Sufficient X-ray data were collected for a connectivity study to confirm the cation to be the same as in **1**. Formation of the cation is summarized in eqn (2).

$$2Fe(NO_3)_3 + 2bphnH_2 + H_2O \rightarrow [Fe_2O(bphnH)(bphnH_2)]^{3+} + 3H^+ + 6NO_3^- \quad (2)$$

The two unbound alcohol arms in the Fe_2 cation of **1** suggested that a higher nuclearity complex might form if they could be involved in ligation to Fe^{III} ions. We thus explored various reaction systems with increased Fe : $bphnH_2$ and $bphnH_2$: NEt_3 ratios, and success was achieved with the reaction of $Fe(NO_3)_3$, $bphnH_2$, and NEt_3 in a 2 : 1 : 1 molar ratio in

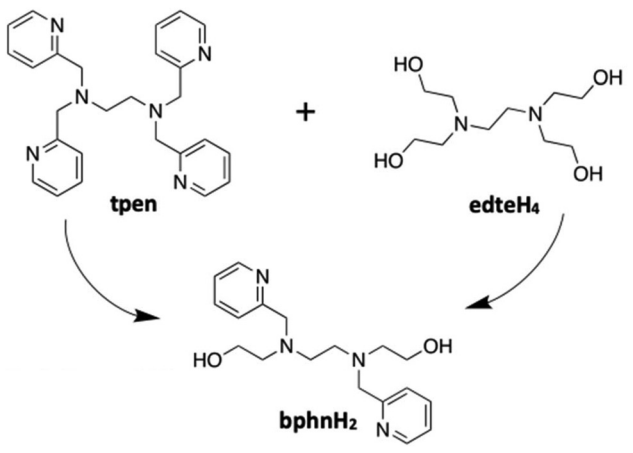

Scheme 1 Diagrammatic representation of the structural relationship between the hexadentate chelates tpen and $edteH_4$ and their hybrid $bphnH_2$ synthesized in this work.

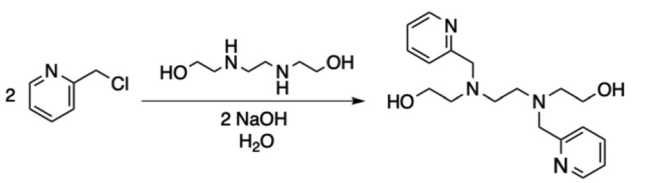

Scheme 2 Procedure for the synthesis of $bphnH_2$. The HCl from 2-picoylchloride is omitted for clarity.

refluxing MeOH. This gave an orange-red solution and subsequent isolation of dark orange-red needle-like crystals of $[Fe_4O(bphn)_2(NO_3)_4](NO_3)_2$ (**2**) in 37% yield. Formation of the cation is summarized in eqn (3).

$$4Fe(NO_3)_3 + 2bphnH_2 + H_2O \rightarrow [Fe_4O(bphn)_2(NO_3)_4](NO_3)_2 + 6H^+ + 6NO_3^- \quad (3)$$

Description of structures

Complex **1**·*x*MeOH crystallizes in orthorhombic space group $P2_12_12_1$ with the Fe_2 cation in a general position. The structure of the cation and its labelled core are shown in Fig. 1 and consist of two distorted-octahedral Fe^{3+} ions bridged only by a μ-O^{2-} ion. The other five coordination sites at each Fe are occupied by a $bphnH_x$ group binding as a pentadentate chelate with one alcohol arm unbound. Dinuclear Fe^{III} complexes with a single O^{2-} bridge usually have a large, often near-linear Fe–O–Fe angle, so the Fe1–O1–Fe2 = 132.19(18)° is surprisingly small, and we thought initially that it might be a μ-HO^-. However, its O bond valence sum (BVS) of 1.81 clearly indicated an O^{2-} ion (Table 2), and we realized the bridging angle is decreased by the close approach of O2 and O3 (2.376 (6) Å) indicating a strong O–H···O hydrogen-bond between them and that one of O atoms is protonated. This was confirmed by the O2 and O3 BVS values of 1.51 and 1.41, respectively, which are in-between those expected for HO^- and O^{2-}

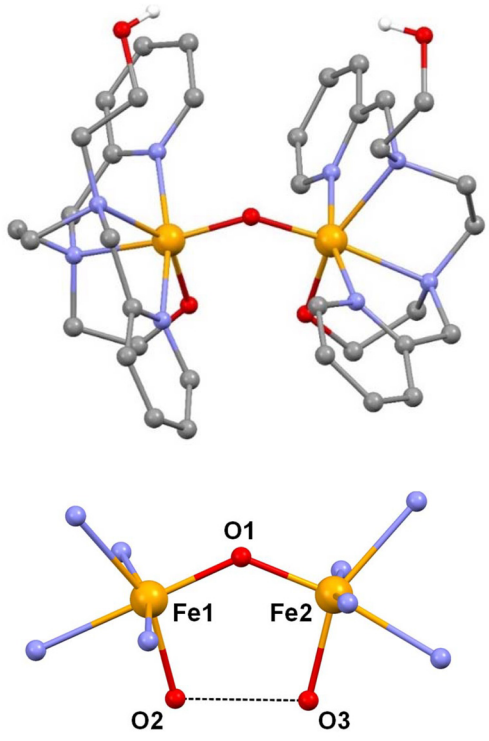

Fig. 1 (Top) Complete structure of the Fe_2 cation of **1** with all except two H atoms omitted for clarity. (Bottom) Partially labelled core with the hydrogen-bond indicated as a black dashed line. Colour code: Fe gold; O red; N blue; C grey; H white.

Table 2 Bond valence sum (BVS) calculations for core O atoms in **1** and **2**

Complex	Atom	BVS	Assignment[a]
1	O1	1.81	O^{2-}
	O2	1.51	O^{2-}/HO^- [b]
	O3	1.41	O^{2-}/HO^- [b]
2	O1	1.79	O^{2-}
	O2	2.04	RO^-
	O3	2.02	RO^-
	O4	1.91	RO^-
	O5	2.05	RO^-

[a] Oxygen BVS values of approx 1.8–2.0, 1.0–1.2, and 0.2–0.4 indicate non-, single-, and double-protonation, respectively, but the values can be affected by hydrogen-bonding. [b] Involved in hydrogen-bonding.

and suggest a ~50% disorder of the H^+ between O2 and O3 (Table 2). The cation formula is thus $[Fe_2O(bphnH)(bphnH_2)]^{3+}$. The Ce^{III} and Fe^{III} oxidation states were confirmed by BVS (Table S1). The $[Ce(NO_3)_6]^{3-}$ contains a dodecacoordinate Ce^{III} comprising six chelating NO_3^- ligands at octahedral positions about the metal. Finally, the two –OH (O4 and O5) of the unbound alcohol arms of the cation are each hydrogen-bonded to different O atoms of the same NO_3^- of the $[Ce(NO_3)_6]^{3-}$ anion (O4···O14 = 2.939(6) and O5···O13 = 2.929(6) Å) (Fig. S1).

Complex **2**·*x*MeOH crystallizes in triclinic space group $P\bar{1}$ with the Fe_4 cation in a general position. As in **1**, all Fe ions are again distorted-octahedral and Fe^{III} (Table S1), whereas the four chelates are now $bphn^{2-}$, *i.e.*, all their alcohol arms (O2–O5) are deprotonated (Table 2). The resulting Fe/O core possesses an unprecedented structure to our knowledge. The four Fe^{III} ions form an almost perfect rhombus with the four alkoxide arms each bridging an edge; the Fe···Fe distances and Fe–O–Fe angles are 3.311(1)–3.385(1) Å and 113.55(12)–117.74 (12)°, respectively. In addition, the shorter next-nearest Fe3/Fe4 pair is bridged by a μ-O^{2-} (O1), confirmed by O BVS (Table 2), with a near-linear Fe3–O1–Fe4 = 176.0(2)° angle.

The $\{Fe_4(\mu\text{-}O^{2-})\}$ unit is essentially planar (maximum deviation = 0.019 Å by Fe3 and Fe4), whereas the edge-bridging alkoxides alternate above and below this plane (Fig. 2), giving a twist angle of 24.4° between the two halves of the core and virtual D_2 symmetry. Peripheral ligation is completed at Fe1 and Fe3 by the $bphn^{2-}$ chelates whereas that at Fe2 and Fe4 is by two NO_3^- groups each. The complete molecule also has virtual D_2 symmetry if ligand disorder and differing binding modes for the NO_3^- ligands are ignored (Fig. 3).

Magnetic susceptibility studies

DC magnetic susceptibility (χ_M) data were collected on vacuum-dried, lightly-ground samples of 1·2MeOH and **2**, restrained in eicosane to avoid torquing, in the 5.0–300 K temperature range and in a 0.1 T applied DC field. The data are plotted as $\chi_M T$ *vs.* *T*. For 1·2MeOH, $\chi_M T$ decreases steadily from 2.26 cm^3 K mol^{-1} at 300 K to 0.39 cm^3 K mol^{-1} at 5.0 K (Fig. 4).

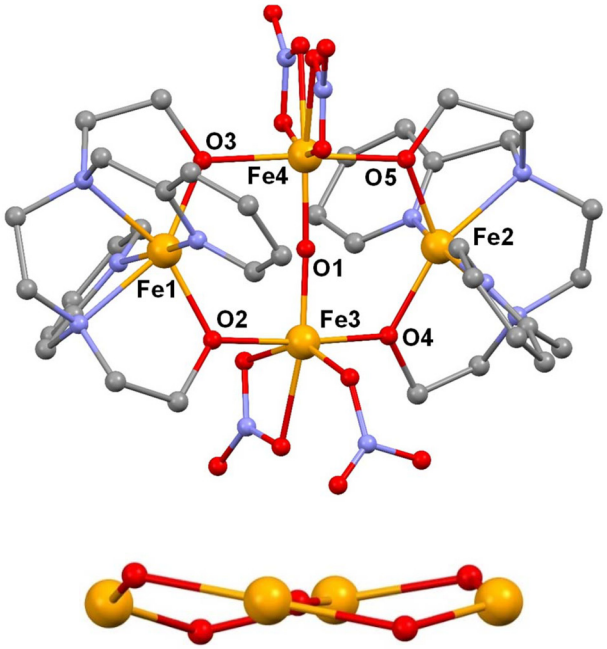

Fig. 2 (Top) Partially labelled structure of the cation of 2. (Bottom) Side-view of the core to emphasize the planar {$Fe_4(\mu\text{-}O^{2-})$} unit, the alkoxide O atoms above and below the plane, and the overall twisted nature of the complete core. Colour code: Fe gold; O red; N blue; C grey.

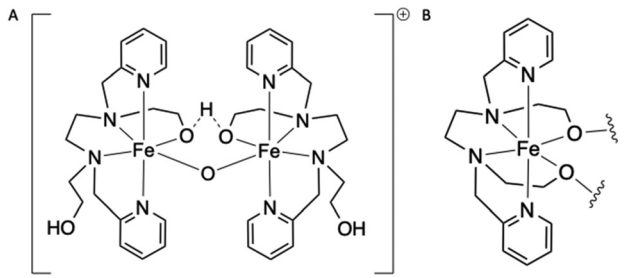

Fig. 3 Illustration of the coordination modes of $bphnH_x$ in the cations of **1** and **2**. (A) Cation of **1** showing hydrogen-bonding between the ethanol/ethoxy arms of the $bphnH_x$. (B) One half of the cation of **2** showing the $bphn^{2-}$ chelation around Fe.

The 300 K value is much lower than the 9.56 cm^3 K mol^{-1} calculated for two high-spin Fe^{III} with $g = 2$ (8.75 cm^3 K mol^{-1}) and one Ce^{III} (f^1 free-ion: $S = \frac{1}{2}$, $L = 3$, $^2F_{5/2}$, $\chi_M T = 0.81$ cm^3 K mol^{-1}) non-interacting ions. This indicates strong AF exchange interactions between the two Fe^{III} ions and a resulting $S = 0$ ground state for the Fe_2 unit, consistent with the steady decrease in $\chi_M T$ with decreasing T and a non-zero $\chi_M T$ at 5.0 K from the Ce^{III} counterion. A fit of the data gave $J = -50.7$ (8) cm^{-1} ($\hat{H} = -2J_{ij}\hat{S}_i \cdot \hat{S}_j$ convention), with fixed $g = 2.0$ and temperature independent paramagnetism (TIP) of 100×10^{-6} cm^3 per mol per Fe.

For **2**, $\chi_M T$ decreases only slowly from 8.55 cm^3 K mol^{-1} at 300 K to 7.55 cm^3 K mol^{-1} at 80.0 K and then more rapidly to

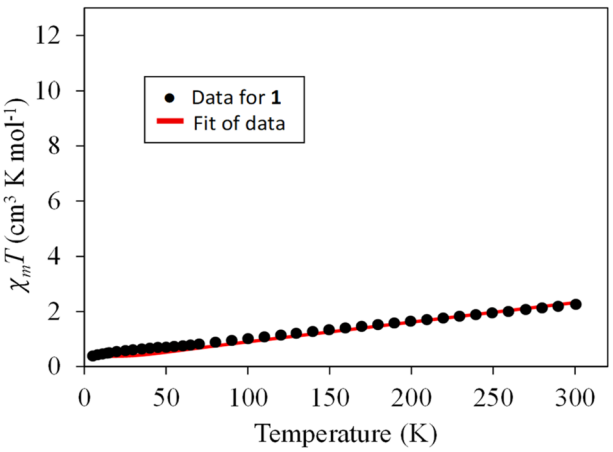

Fig. 4 $\chi_M T$ *vs.* T plot for complex **1**·2MeOH in a 0.1 T dc field. The red line is the fit of the data to a dinuclear Fe^{III} unit with a constant $g = 2.0$.

2.62 cm^3 K mol^{-1} at 5.0 K (Fig. 5). The 300 K value is much smaller than the spin-only ($g = 2$) value for four non-interacting Fe^{III} ions (17.50 cm^3 K mol^{-1}) again indicating dominant **AF** interactions with one (or more) being particularly strong. The rapidly decreasing $\chi_M T$ at the lowest T suggests an $S = 0$ ground state.

The unusual $\chi_M T$ *vs.* T profile for **2** can be qualitatively rationalized by consideration of the various couplings (J_{ij}) within the core (Fig. 4, inset). The $\chi_M T$ at 300 K and its only slight decrease with decreasing T down to 70 K is consistent with two Fe^{III} spins being nearly paired up by 300 K by a strong **AF** interaction ($\chi_M T$ for two Fe^{III} ions is 8.75 cm^3 K mol^{-1}). Consistent with this is the J_{34} coupling across the near-linear Fe3–O–Fe4 bridge, the large Fe–O–Fe angle being expected to lead to a very strong interaction. If this interpretation is correct, the 70–300 K data reflect Fe1 and Fe2 interacting with an almost diamagnetic {Fe_2O_5} unit containing Fe3

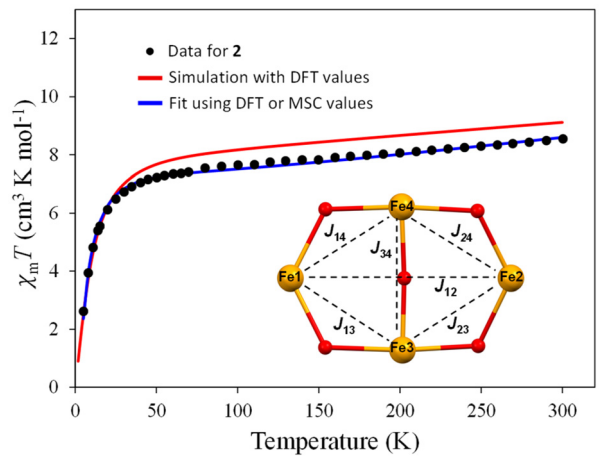

Fig. 5 Plot of experimental $\chi_M T$ *vs.* T data (●) for complex **2** in the 5.0–300 K range in a 0.1 T DC field. The red line is the simulation using the DFT values as inputs, and the blue line is the fit using either MSC or DFT inputs.

and Fe4. The steep decrease below ~50 K would then be due to any long-range J_{12} coupling by superexchange pathways, *via* four-bonds through Fe3 or Fe4, *via* two weak Fe···O interactions through central O1, or both. This analysis represents a reasonable rationalization of the $\chi_M T$ *vs.* T plot for **2** in Fig. 5, but it needed to be tested quantitatively by determination of the various J_{ij} values. We thus carried out the latter using our three-pronged approach involving fits of experimental data, DFT calculations, and use of our MSC for Fe^{III}/O clusters.

Applying virtual D_2 core symmetry, the exchange coupling within the Fe_4 rhombus is a 3-J system described by the Heisenberg–Dirac–Van Vleck (HDVV) spin Hamiltonian of eqn (4), where $J = J_{13} = J_{14} = J_{23} = J_{24}$, $J' = J_{34}$ and $J'' = J_{12}$ (Fig. 5); the subscripts are the Fe atom labels. This can be converted into an equivalent form using the substitutions $\hat{S}_A = \hat{S}_3 + \hat{S}_4$, $\hat{S}_B = \hat{S}_1 + \hat{S}_2$, and $\hat{S}_T = \hat{S}_A + \hat{S}_B$, where $\hat{S}_T$ is the total spin of the molecule, leading to the energy expression of eqn (5),

$$\mathcal{H} = -2J(\hat{S}_1 \cdot \hat{S}_3 + \hat{S}_1 \cdot \hat{S}_4 + \hat{S}_2 \cdot \hat{S}_3 + \hat{S}_2 \cdot \hat{S}_4) - 2J'(\hat{S}_3 \cdot \hat{S}_4) - 2J''(\hat{S}_1 \cdot \hat{S}_2) \quad (4)$$

$$E|S_T, S_A, S_B\rangle = -J[S_T(S_T+1) - S_A(S_A+1) - S_B(S_B+1)] - J'[S_A(S_A+1)] - J''[S_B(S_B+1)] \quad (5)$$

with constant values omitted, where $E|S_T, S_A, S_B\rangle$ is the energy of a state S_T arising from particular S_A and S_B values.

Listed in Table 3 are the J_{MSC}, J_{DFT}, and J_{FIT} values obtained from the three independent approaches for **2** with imposed virtual D_2 symmetry. MSC refers to the semi-empirical Mitchell–Christou magnetostructural procedure of eqn (6)[29] developed specifically for higher nuclearity Fe^{III}/O clusters to estimate the J_{ij} for each Fe_2 pair of **2** from the average Fe–O bond length (r) and Fe–O–Fe angle (φ) at the monoatomic bridging O atom. As we have found previously for several Fe_x (x = 5–36) clusters, the estimates from the three approaches are generally in agreement with the following approximate ranges of J_{ij}: weak (0 to −10 cm^{-1}), medium (−10 to −25 cm^{-1}), and strong (> −25 cm^{-1}).

$$J_{MSC} = (1.23 \times 10^9)(-0.12 + 1.57\cos\varphi + \cos^2\varphi)e^{-8.99r} \quad (6)$$

In fact, J' (J_{34}) is very strong and confirms that the near-linear Fe–O–Fe is responsible for the $\chi_M T$ at 300 K being so small. The J_{DFT} give a reasonable simulation of the experimental $\chi_M T$ *vs.* T data (red line in Fig. 4), but the J_{MSC} give a poorer simulation at lower temperatures (Fig. S2) indicating the J_{12} value to be significantly underestimated by the MSC. Nevertheless, using either the J_{MSC} or the J_{DFT} values as inputs gave the same excellent fit (blue line in Fig. 5, and Table 3). This is consistent with our prior experience that using J_{MSC} or J_{DFT} estimates as inputs for fits of experimental data greatly helps avoid false fits due to over-parameterization, even for only a 3-J system. We also explored this in the present case by using inputs of 0, −10, and −20 cm^{-1}. Excellent fits were obtained in each case, but those for the 0 and −10 cm^{-1} inputs were clearly unreasonable, giving massive ferromagnetic and antiferromagnetic couplings, whereas the −20 cm^{-1} inputs gave the same fit as the J_{MSC} and J_{DFT} inputs. We also probed whether the weak J'' (J_{12}) fit value was reliable given that it was part of a 3-J fit with two much stronger interactions. We thus fit only the low-T data to J'', and data in the 5.0–100 K and 5.0–50 K ranges gave −0.75 and −0.71 cm^{-1}, respectively, (Fig. S3) supporting the conclusion from the 3-J fit of the 5.0–300 K data.

The MSC and DFT calculations lead to individual values, of course, for the four J interactions, J_{13}, J_{14}, J_{23}, and J_{24}. These were averaged under virtual D_2 symmetry in Table 3 but are given individually in Table S2. The latter also shows that excellent fits obtained using J_{MSC} and J_{DFT} inputs now do not give the same fit values, consistent with overparameterization problems. The same situation was obtained using only ≥70 K data to omit the lower T drop and exclude J_{12} (Fig. S5), and with inputs of 0, −10 and −20 cm^{-1}. The AC in-phase $\chi'_M T$ *vs.* T data for **2** (Fig. 6) show a steadily decreasing $\chi'_M T$ from 0.52 cm^3 K mol^{-1} at 15 K to 0.36 cm^3 K mol^{-1} at 1.8 K and clearly heading for zero at 0 K, in good agreement with the dc susceptibility data and confirming an S = 0 ground state. Fitting of these data to a dinuclear Fe^{III} unit provided an independent determination of J'' (J_{12}) that precluded any complications from a DC field, giving J'' (J_{12}) = −0.61 cm^{-1}, in satisfying agreement with the DC fit.

Finally, we note that Fe_4 complex **2** is a magnetically very interesting 3-J system because the magnitudes of its three types of J_{ij} couplings are very different and affect the $\chi'_M T$ *vs.* T data in nearly independent T ranges. The latter also means that although **2** has a structure comprising two isosceles triangles sharing the unique edge and all the J_{ij} are AF, it does not show spin frustration effects arising from competing interactions of comparable magnitude that often lead to $S \neq 0$ ground states for even nuclearity clusters. In **2**, the competing interactions are not of comparable magnitude, and the ground state is S = 0.

Table 3 Exchange interactions J, J' and J'' for **2** from MSC calculations, DFT computations, and PHI fits of experimental DC data with various input values

J_{ij} [a]	J_{MSC}	J_{DFT}	$J_{FIT(M)}$ [b]	$J_{FIT(D)}$ [c]	J_{FIT} (0)[d]	J_{FIT} (−10)[d]	J_{FIT} (−20)[d]
J	−14.5[e]	−7.3[f]	−11.3	−11.3	−71.2	−71.3	−11.3
J' (J_{34})	−75.6[e]	−78.4[f]	−57.1	−57.1	−203	−203	−57.1
J'' (J_{12})	−0.01	−0.6	−1.1	−1.1	+299	+260	−1.1
TIP[g]	—	—	400	400	400	400	400

[a] cm^{-1}. [b] J_{MSC} as fit inputs. [c] J_{DFT} as fit inputs. [d] Numbers in parentheses are input values for the fits. [e] Average of four MSC values in the −13.6 to −14.9 cm^{-1} range. [f] Average of four DFT values in the −4.8 to −9.4 cm^{-1} range. [g] ×10^{-6} cm^3 K mol^{-1}.

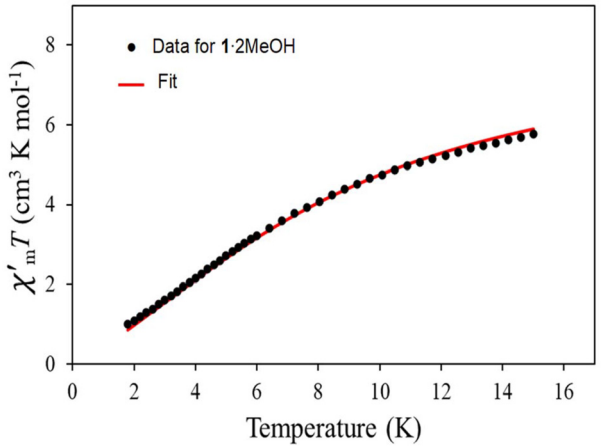

Fig. 6 Plot of experimental AC in-phase $\chi'_M T$ *vs.* *T* data (●) for complex **2** in the 1.8–15 K range in a 3.5 G AC field at a 1000 Hz oscillation frequency. The red line is the fit to the dinuclear Fe1···Fe2 unit; see the text for the *J*″ (J_{12}) fit value.

Conclusions

The new bphnH$_2$ molecule with a mixed diol/diamine/dipyridine nature has proven on partial or complete deprotonation to be a source of two new Fe^{III}/oxo complexes with unprecedented structures. Complexes **1** and **2** contain pentadentate bphnH$^-$ and hexadentate bphn^{2-}, respectively, and will likely prove a rich source of other metal clusters in the future. We note that our three-pronged approach to studying Fe/O clusters, namely, MSC, DFT, and fits of experimental data, has once again revealed satisfying agreement between them for **2** and a resulting detailed analysis of its interactions and reliability of fits, including for the very weak long-range interaction between Fe1 and Fe2. Further applications of this three-pronged approach to other clusters are in progress.

Author contributions

AD, synthesis **1** and **2**, design and synthesis of bphnH$_2$, magnetic data collection and analysis, manuscript 1st draft. AF, synthesis of bphnH$_2$. CLB, LD, and KAA, X-ray crystallographic studies; JEP, DFT computations; GC, supervision, manuscript completion, project administration, funding acquisition.

Conflicts of interest

There are no conflicts to declare.

Data availability

Supporting data has been provided as part of the supplementary information (SI). Supplementary information: additional figure of **1** and its anion; Fe and Ce bond valence sum tables; additional magnetism plots for **2**; and tables of magnetic data and fits. See DOI: https://doi.org/10.1039/d6dt01053a.

CCDC 2551518 and 2551519 contain the supplementary crystallographic data for this paper.[53a,b]

Acknowledgements

This work was supported by the US Department of Energy, Office of Basic Energy Sciences, as part of the Computational Chemical Sciences Program under award #DESC0018331.

References

1 K. Weighardt, K. Pohl, I. Jibril and G. Huttner, *Angew. Chem., Int. Ed. Engl.*, 1984, **23**, 77–78.
2 A. L. Barra, P. Debrunner, D. Gatteschi, E. S. Ch and R. Sessoli, *Europhys. Lett.*, 1996, **35**, 133.
3 A. L. Barra, A. Caneschi, A. Cornia, F. Fabrizi de Biani, D. Gatteschi, C. Sangregorio, R. Sessoli and L. Sorace, *J. Am. Chem. Soc.*, 1999, **121**, 5302–5310.
4 A. K. Boudalis, B. Donnadieu, V. Nastopoulos, J. M. Clemente-Juan, A. Mari, Y. Sanakis, J.-P. Tuchagues and S. P. Perlepes, *Angew. Chem., Int. Ed.*, 2004, **43**, 2266–2270.
5 S. Accorsi, A.-L. Barra, A. Caneschi, G. Chastanet, A. Cornia, A. C. Fabretti, D. Gatteschi, C. Mortalò, E. Olivieri, F. Parenti, P. Rosa, R. Sessoli, L. Sorace, W. Wernsdorfer and L. Zobbi, *J. Am. Chem. Soc.*, 2006, **128**, 4742–4755.
6 C. Schlegel, E. Burzurí, F. Luis, F. Moro, M. Manoli, E. K. Brechin, M. Murrie and J. van Slageren, *Chem. – Eur. J.*, 2010, **16**, 10178–10185.
7 Y.-Y. Zhu, C. Cui, K. Qian, J. Yin, B.-W. Wang, Z.-M. Wang and S. Gao, *Dalton Trans.*, 2014, **43**, 11897–11907.
8 L. Rigamonti, M. Piccioli, A. Nava, L. Malavolti, B. Cortigiani, R. Sessoli and A. Cornia, *Polyhedron*, 2017, **128**, 9–17.
9 S. Liu, Y.-F. Deng, C. A. Li, X. Chang and Y.-Z. Zhang, *Dalton Trans.*, 2018, **47**, 16704–16708.
10 P. Waghmodey, A. K. Singh, H. Khalilullah and A. Verma, *Biomed. Mater. Devices*, 2026, DOI: 10.1007/s44174-026-00662-9.
11 M. Sankaralingam and M. Palaniandavar, *Polyhedron*, 2014, **67**, 171–180.
12 M. Costas, J.-U. Rohde, A. Stubna, R. Y. N. Ho, L. Quaroni, E. Münck and L. Que, *J. Am. Chem. Soc.*, 2001, **123**, 12931–12932.
13 D. Coucouvanis, R. A. Reynolds III and W. R. Dunham, *J. Am. Chem. Soc.*, 1995, **117**, 7570–7571.
14 K. Kim and S. J. Lippard, *J. Am. Chem. Soc.*, 1996, **118**, 4914–4915.
15 D. Lee and S. J. Lippard, *J. Am. Chem. Soc.*, 1998, **120**, 12153–12154.
16 S. Herold and S. J. Lippard, *J. Am. Chem. Soc.*, 1997, **119**, 145–156.

17 S. Menage, Y. Zang, M. P. Hendrich and L. Que Jr, *J. Am. Chem. Soc.*, 1992, **114**, 7786–7792.
18 S. Menage, B. A. Brennan, C. Juarez-Garcia, E. Munck and L. Que Jr, *J. Am. Chem. Soc.*, 1990, **112**, 6423–6425.
19 B. Mauerer, J. Crane, J. Schuler, K. Wieghardt and B. Nuber, *Angew. Chem., Int. Ed. Engl.*, 1993, **32**, 289–291.
20 H. Arii, S. Nagatomo, T. Kitagawa, T. Miwa, K. Jitsukawa, H. Einaga and H. Masuda, *J. Inorg. Biochem.*, 2000, **82**, 153–162.
21 K. H. K. Lee, L. Aebersold, J. E. Peralta, K. A. Abboud and G. Christou, *Inorg. Chem.*, 2022, **61**, 17256–17267.
22 R. Bagai, K. A. Abboud and G. Christou, *Chem. Commun.*, 2007, 3361.
23 R. Bagai, S. Datta, A. Betancur-Rodriguez, K. A. Abboud, S. Hill and G. Christou, *Inorg. Chem.*, 2007, **46**, 4535–4547.
24 R. Bagai, M. R. Daniels, K. A. Abboud and G. Christou, *Inorg. Chem.*, 2008, **47**, 3318–3327.
25 R. Bagai, K. A. Abboud and G. Christou, *Inorg. Chem.*, 2007, **46**, 5567–5575.
26 A. R. Hale, M. E. Lott, J. E. Peralta, D. Foguet-Albiol, K. A. Abboud and G. Christou, *Inorg. Chem.*, 2022, **61**, 11261–11276.
27 S. Datta, A. Betancur-Rodriguez, S.-C. Lee, S. Hill, D. Foguet-Albiol, R. Bagai and G. Christou, *Polyhedron*, 2007, **26**, 2243–2246.
28 D. Foguet-Albiol, K. A. Abboud and G. Christou, *Chem. Commun.*, 2005, 4284.
29 K. J. Mitchell, K. A. Abboud and G. Christou, *Inorg. Chem.*, 2016, **55**, 6597–6608.
30 A. P. Singh, R. P. Joshi, K. A. Abboud, J. E. Peralta and G. Christou, *Polyhedron*, 2020, **176**, 114182.
31 J. Lengyel, S. A. Stoian, N. Dalal and M. Shatruk, *Polyhedron*, 2018, **151**, 446–451.
32 K. H. K. Lee, J. E. Peralta, K. A. Abboud and G. Christou, *Inorg. Chem.*, 2020, **59**, 18090–18101.
33 A. A. Kitos, C. Papatriantafyllopoulou, A. J. Tasiopoulos, S. P. Perlepes, A. Escuer and V. Nastopoulos, *Dalton Trans.*, 2017, **46**, 3240–3251.
34 D. Gatteschi, R. Sessoli and A. Cornia, *Chem. Commun.*, 2000, 732.
35 L. Arizaga, W. Cañon-Mancisidor, J. S. Gancheff, R. A. Burrow, D. Armentano, F. Lloret, R. González, C. Kremer and R. Chiozzone, *Polyhedron*, 2019, **174**, 114165.
36 G. Sheldrick, *Acta Crystallogr., Sect. C:Struct. Chem.*, 2015, **71**, 3–8.
37 A. Spek, *Acta Crystallogr., Sect. C:Struct. Chem.*, 2015, **71**, 9–18.
38 N. F. Chilton, R. P. Anderson, L. D. Turner, A. Soncini and K. S. Murray, *J. Comput. Chem.*, 2013, **34**, 1164–1175.
39 W. Liu and H. H. Thorp, *Inorg. Chem.*, 1993, **32**, 4102–4105.
40 I. D. Brown, *Chem. Rev.*, 2009, **109**, 6858–6919.
41 M. J. Frisch, G. W. Trucks, H. B. Schlegel, G. E. Scuseria, M. A. Robb, J. R. Cheeseman, G. Scalmani, V. Barone, G. A. Petersson, H. Nakatsuji, X. Li, M. Caricato, A. V. Marenich, J. Bloino, B. G. Janesko, R. Gomperts, B. Mennucci, H. P. Hratchian, J. V. Ortiz, A. F. Izmaylov, J. L. Sonnenberg, G. Williams, F. Ding, F. Lipparini, F. Egidi, J. Goings, B. Peng, A. Petrone, T. Henderson, D. Ranasinghe, V. G. Zakrzewski, J. Gao, N. Rega, G. Zheng, W. Liang, M. Hada, M. Ehara, K. Toyota, R. Fukuda, J. Hasegawa, M. Ishida, T. Nakajima, Y. Honda, O. Kitao, H. Nakai, T. Vreven, K. Throssell, J. A. Montgomery Jr, J. E. Peralta, F. Ogliaro, M. J. Bearpark, J. J. Heyd, E. N. Brothers, K. N. Kudin, V. N. Staroverov, T. A. Keith, R. Kobayashi, J. Normand, K. Raghavachari, A. P. Rendell, J. C. Burant, S. S. Iyengar, J. Tomasi, M. Cossi, J. M. Millam, M. Klene, C. Adamo, R. Cammi, J. W. Ochterski, R. L. Martin, K. Morokuma, O. Farkas, J. B. Foresman and D. J. Fox, *Gaussian 16 Rev. C.01*, Wallingford, CT, 2016.
42 C. van Wüllen, *J. Phys. Chem. A*, 2009, **113**, 11535–11540.
43 E. Ruiz, A. Rodríguez-Fortea, J. Cano, S. Alvarez and P. Alemany, *J. Comput. Chem.*, 2003, **24**, 982–989.
44 P. Comba, S. Hausberg and B. Martin, *J. Phys. Chem. A*, 2009, **113**, 6751–6755.
45 A. Bencini, F. Totti, C. A. Daul, K. Doclo, P. Fantucci and V. Barone, *Inorg. Chem.*, 1997, **36**, 5022–5030.
46 R. Valero, R. Costa, I. de P. R. Moreira, D. G. Truhlar and F. Illas, *J. Chem. Phys.*, 2008, **128**, 114103.
47 J. J. Phillips and J. E. Peralta, *J. Chem. Theory Comput.*, 2012, **8**, 3147–3158.
48 R. P. Joshi, J. J. Phillips and J. E. Peralta, *J. Chem. Theory Comput.*, 2016, **12**, 1728–1734.
49 R. Bagai, K. A. Abboud and G. Christou, *Inorg. Chem.*, 2008, **47**, 621–631.
50 S. Pal, J. W. Gohdes, W. C. A. Wilisch and W. H. Armstrong, *Inorg. Chem.*, 1992, **31**, 713–716.
51 J. W. Shin, S. R. Rowthu, M. Y. Hyun, Y. J. Song, C. Kim, B. G. Kim and K. S. Min, *Dalton Trans.*, 2011, **40**, 5762–5773.
52 J. M. Botha, K. Umakoshi, Y. Sasaki and G. J. Lamprecht, *Inorg. Chem.*, 1998, **37**, 1609–1615.
53 (*a*) CCDC 2551518: Experimental Crystal Structure Determination, 2026, DOI: 10.5517/ccdc.csd.cc2rn21k; (*b*) CCDC 2551519: Experimental Crystal Structure Determination, 2026, DOI: 10.5517/ccdc.csd.cc2rn22l.